



Heteroatom-doped porous carbon derived from covalent organic framework for high performance supercapacitor applications

Yuzhu Xing¹ · Yan Dong¹ · Jifan Zhao¹ · Zhiqiang Zhang¹ · Yue Wang¹

Received: 19 January 2023 / Revised: 29 May 2023 / Accepted: 1 June 2023 / Published online: 20 June 2023
© The Author(s), under exclusive licence to Korean Carbon Society 2023

Abstract

In recent years, supercapacitors have attracted extensive attention due to their advantages such as fast charge and discharge rate, high power density and long cycle life. Because of its unique porous structure and excellent electrochemical properties, heteroatom-doped porous carbon (HPC) is deemed as a promising electrode material for supercapacitors. However, it is a great challenge to synthesize electrode materials with large surface area, ultra-high porosity and good electrochemical performance. In this work, two-dimensional conjugated microporous polymers (CMPs) containing ketones were synthesized by a simple one-step coupling reaction and used as carbon precursors. A series of samples (CMP-Ts) were prepared with the procedures of coupling reaction and carbonization. The optimized carbon material has high specific surface area (up to 2229.85 m² g⁻¹), porous structure, high specific capacitance (375 F g⁻¹ at 0.5 A g⁻¹), and good cycling stability (capacitance retention of 98.8% after 1000 cycles at 5 A g⁻¹). Further, the supercapacitor has an energy density of 28.8 Wh kg⁻¹ at a power density of 5000 W kg⁻¹. This work lays a foundation for the preparation of carbon materials using microporous polymer as a precursor system, provides a new way of thinking, and demonstrates a great potential of high-performance supercapacitors.

Keywords Supercapacitors · Conjugated microporous polymer · Covalent organic framework

1 Introduction

With the increasing consumption of non-renewable resources, the demand in energy and sustainable environment have become a principal consideration worldwide. The growing environmental pollution problems from regular uses of fossil fuels also have promoted a major research attention on the consideration of environment-friendly [1]. In recent years, supercapacitors (SCs) have become an excellent energy storage device due to their advantages of rapid charge–discharge, high power density and long cycle life, etc. Meanwhile, they are also well applied in power transmission, regenerative braking and other fields [2, 3]. SCs can be divided into two categories according to their working principle, pseudocapacitor and

electric double layer supercapacitor (EDLC) [4]. Among them, the unique electrochemical performance of electric double-layer supercapacitor makes it widely used in various electronic devices, and its electrical storage capacity is mainly affected by the size of pore volume and specific surface area of electrode materials [5]. Up to date, many materials with different structures [6–12] are utilized as the electrode in supercapacitors and batteries [13–15]. Among these candidates, porous carbon materials are the most widely used electrode material for EDLC due to their distinctive structural advantages as follows: Firstly, the porous structure can provide more active sites for charge. Secondly, the porous structure can provide a large specific surface area for electron transport [16]. High-performance porous carbon materials should be characterized by high conductivity, high charge transport capacity, large surface area and long cycle life [17–19]. In the preparation of porous carbon materials, doping heteroatoms such as boron, oxygen, nitrogen, sulfur and other heteroatoms is also an effective way to further improve the electrochemical performance of supercapacitors [20–25]. These doped heteroatoms are found to be effectively enhance the surface wettability and

✉ Yan Dong
dong_yan168@163.com

✉ Yue Wang
wangyue@ustl.edu.cn

¹ School of Chemical Engineering, University of Science and Technology Liaoning, 185 Qianshan Middle Road, High-Tech Zone, Anshan 114051, Liaoning, China

electrical conductivity of the carbon skeleton and provide active sites for pseudocapacitive charge storing [26–28].

In recent years, researchers have developed large specific surface area porous carbon materials with different structures and pore size distribution according to different preparation methods [29–31]. Among them, conjugated microporous polymers (CMPs) have attracted more and more attention due to their high surface area, excellent thermal and chemical stability and adjustable pore size distribution. The unique π -conjugated framework of CMPs makes it suitable for energy storage and electronic devices, which makes it an excellent candidate for carbon material precursors [32]. Direct carbonization of the precursor is the easiest way to prepare porous carbon materials. The structure of precursor is very important for the performance of porous carbon materials in supercapacitors. CMPs materials are ideal precursors for porous carbon materials due to their inherent porosity, excellent stability, structural controllable performance and high specific surface area [31].

Herein, a series of two-dimensional conjugated microporous polymers (CMPs) were designed and synthesized by a facile one-step coupling reaction using 4,4'-difluorodiphenyl sulfone and 4,4'-dihydroxybenzophenone as the precursor of carbon materials (Fig. 1). By mixing and carbonizing CMPs with KOH, a series of porous carbon materials (CMP-Ts) were obtained. As an electrode material for SCs, the optimized CMP-Ts have excellent performance, high specific capacitance, superior energy and power density, and robust cycle stability. The present work provides a new direction for the preparation of carbon materials using CMP as a precursor and demonstrates a great potential of

carbon materials as electrode materials for high-performance supercapacitors.

2 Methods

2.1 Materials

Unless otherwise noted, commercially available reagents and solvents were used as received without further purification. 4,4'-difluorodiphenyl sulfone (DDS) and 4,4'-dihydroxybenzophenone (DHBP) were purchased from Shanghai Dibai Biotechnology Co., LTD and Shanghai HaoHong Biomedical Technology Co., LTD, respectively. *N,N*-dimethylacetamide (DMAc) was purchased from Tianjin Fengchuan Chemical Reagent Technology Co., LTD. Anhydrous potassium carbonate (K_2CO_3) was supplied by Shanghai Maclin Biochemical Technology Co., LTD. Potassium hydroxide (KOH) was provided by Shanghai Aladdin Biochemical Technology Co., LTD. Anhydrous ethanol was purchased from Tianjin Opusen Chemical Co., LTD. Polytetrafluoroethylene (PTFE) aqueous solution was purchased from Minnesota Mining & Machine Manufacturing Corporation. Conductive carbon black was purchased from Cabot Corporation, USA. Foamed nickel (200 mm \times 300 mm \times 2 mm) was purchased from Kunshan Guangjiayuan New Material Co., LTD. 6 M KOH aqueous solution was used as the electrolyte for electrochemical measurements.

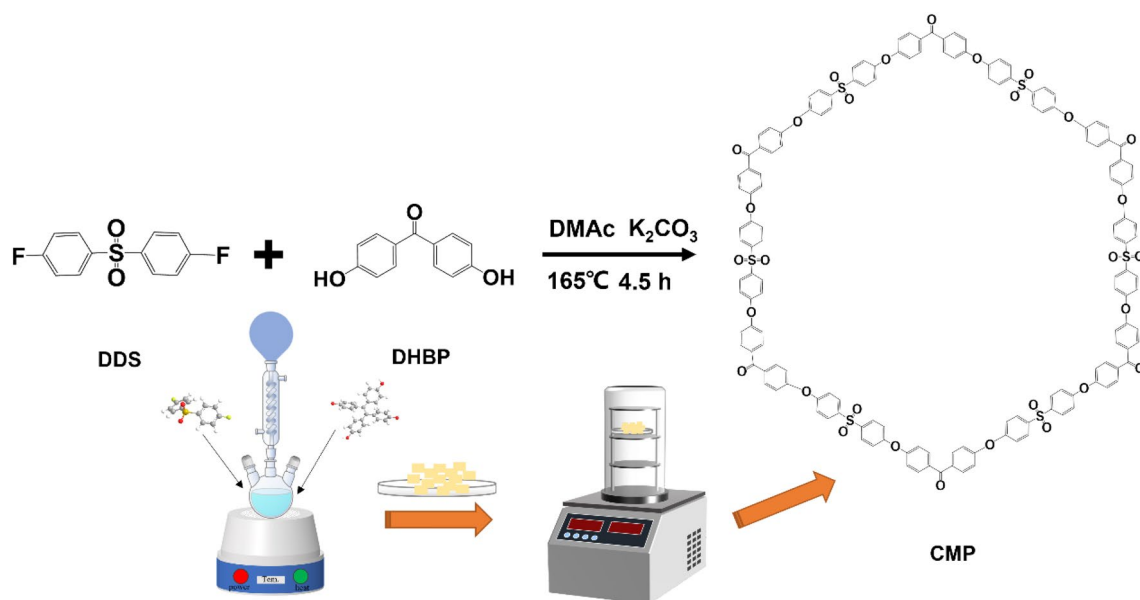


Fig. 1 Schematic illustration of the preparation of CMP

2.2 Preparation of CMPs

4, 4'-difluorodiphenyl sulfone (DDS) (250 mg, 1 mmol), 4,4'-dihydroxybenzophenone (DHBP) (214 mg, 1 mmol), anhydrous potassium carbonate (K_2CO_3) (310 mg, 2.25 mmol), and *N,N*-dimethylacetamide (10 mL) were added to a round bottom flask under nitrogen atmosphere. The resulting suspension was heated to 165 °C under reflux for 4.5 h. The resulting yellow solution was collected by filtration and washed with DMAc (2×15 mL) and deionized water (2×30 mL), respectively. After drying at 80 °C under vacuum for 24 h, pale yellow pieces were obtained in 82% (349 mg) isolated yield.

2.3 Carbonization procedure of CMP-Ts

400 mg of well-grinded potassium hydroxide (KOH) and 200 mg of CMP were mixed and pyrolyzed at various temperatures for 1 h in a horizontal tube furnace under nitrogen atmosphere with a flow rate of 60 mL min^{-1} . After cooling down to room temperature, the obtained black powder was washed with deionized water until the pH of the solution reached neutral. The black powder was dried at 80 °C for 12 h under vacuum and obtained the final products of CMP-700 (pyrolysis temperature: 700 °C, yield: 80%, 160 mg), CMP-800 (pyrolysis temperature: 800 °C, yield: 75%, 150 mg), and CMP-900 (pyrolysis temperature: 900 °C, yield: 68%, 136 mg).

2.4 Characterizations

Scanning electron microscopy (SEM) images were obtained by using the Zeiss SUPRA 55 SAPPHERE. Transmission electron microscopy (TEM) images were collected on a FEI Tecnai G2 F20 electron microscope. Nitrogen adsorption and desorption isotherms were measured on a Quantachrome Quadrasorb EVO sorption analyzer at 77 K. The Brunauer–Emmett–Teller (BET) method was utilized to calculate the specific surface area (S_{BET}). The pore size distributions were derived from the adsorption branches of isotherms taking advantage of nonlocal density functional theory (NLDFT) method, and total pore volumes (V_{total}) were characterized at relative pressure of 0.99. Micropore surface area and volume were obtained via t-plot analysis. The Raman spectroscopy were carried out on a XploRA PLUS intelligent fully automatic Raman spectrometer produced by HORIBA, Japan. X-ray diffraction measurements were recorded on a PANalytical X'Pert Powder X-ray diffractometer (D8 ADVANCE, Cu-K α , 40 kV, 40 mA, and $\lambda = 1.5418$ Å), 2θ from 5° to 40° with 0.02° increment. Fourier transform infrared spectra (FT-IR) were recorded in the range of 600 to 4000 cm^{-1} on a Nicolet (iS 10, USA) FT-IR spectrometer. X-ray

photoelectron spectroscopy (XPS) were tested on a K-Alpha XPS spectrometer (Thermo Fisher Scientific, Waltham, MA, USA).

2.5 Preparation of supercapacitor electrode

The supercapacitor electrode was prepared by mixing 80 wt% (4 mg) CMP and 20 wt% (0.5 mg) superconductive carbon black. Pour the mixture into a mortar and add 1 drop of PTFE aqueous solution (PTFE: deionized water = 1:9) and 1 drop of ethanol. The suspension was grinded and pasted onto the surface of 1 \times 1 cm Ni-foam. Then, the Ni-foam was pressed with 10 MPa pressure and soaked in 6 M KOH aqueous solution for 12 h.

2.6 Electrochemical measurements

All electrochemical measurements were performed by using a CHI 660E electrochemical workstation (CHI Instruments, China). The experiments were conducted in a 3-electrode system with the sample used as the working electrode, a Pt-foil and a Hg/HgO electrode were the counter and reference electrode, respectively. The used electrolyte was 6 M KOH aqueous solution with performed tests including cyclic voltammetry (CV), galvanostatic charge/discharge (GCD), and electrochemical impedance spectroscopy (EIS).

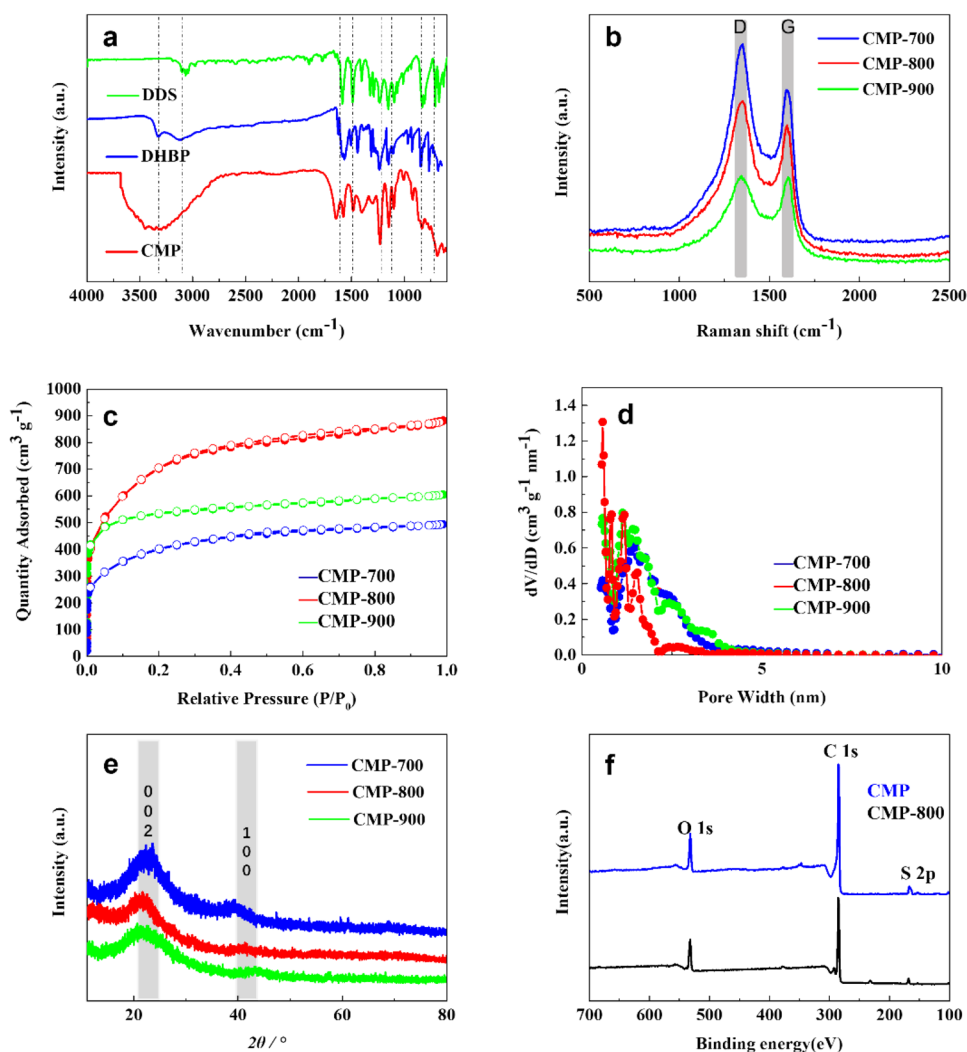
3 Results and discussion

3.1 Synthesis and characterization of CMPs

As shown in Fig. 1, the precursor CMP was synthesized by a simple coupling reaction of 4,4'-difluorodiphenyl sulfone (DDS) and 4,4'-dihydroxybenzophenone (DHBP) under reflux in DMAc in the presence of K_2CO_3 (165 °C, 4.5 h). The polymerization process was progressed in a simple one-step manner. The resulting pale yellow mixture was collected by filtration and washed with DMAc (2×15 mL) and deionized water (2×30 mL), respectively. After freeze drying at -50 °C under vacuum for 24 h, pale yellow pieces were obtained. The top view of synthesized CMP was shown in Fig. S1. Fig. S2 shows the optic image of the synthesized precursor CMP.

The FT-IR spectra of the raw materials DDS, DHBP and synthesized CMP are shown in Fig. 2a. It can be observed that a pair of stretching vibration peaks of benzene ring skeleton appear at 1500 cm^{-1} and 1600 cm^{-1} , and C-H out-of-plane bending vibration peaks appear at 695 cm^{-1} and 830 cm^{-1} . C–H stretching vibration peak appears at 3050 cm^{-1} . The peaks at 1104 cm^{-1} and 1160 cm^{-1} of DDS and CMP are the stretching vibration of S=O bond and C-S bond, respectively. CMP was successfully synthesized with

Fig. 2 **a** FT-IR spectra of the reactants and synthesized CMP. **b** Raman spectra of CMP-700, CMP-800, and CMP-900. **c** N_2 adsorption–desorption isotherms of CMP-700, CMP-800, and CMP-900. **d** Pore size distribution of CMP-700, CMP-800, and CMP-900. **e** XRD patterns of CMP-700, CMP-800, and CMP-900. **f** XPS survey spectra of CMP and CMP-800



the disappearance of stretching vibration peaks of C-F bond in DDS (1300 cm^{-1}) and O-H bond in DHBP (3300 cm^{-1}), and the appearance of stretching vibration peak of Ar-O-Ar bond in CMP (1250 cm^{-1}), stretching vibration peak of C=O bond appeared at 1690 cm^{-1} and the intermolecular hydrogen bond appeared at 3300 cm^{-1} . The surface area and pore size of CMP were studied by nitrogen adsorption/desorption isotherms at 77 K (Fig. S3). At relatively high pressures, the hysteresis loop of N_2 adsorption–desorption isotherms confirms the presence of mesopores in CMP, indicating it is a mesoporous material. In addition, the specific surface area of CMP is $13.53\text{ m}^2\text{ g}^{-1}$, and the total pore volume is $0.015\text{ cm}^3\text{ g}^{-1}$.

3.2 Synthesis and characterization of CMP-Ts based carbons

CMP was carbonized and activated with KOH (KOH: CMP = 2:1) at different temperatures (700, 800, 900°C)

to form samples of CMP-700, CMP-800 and CMP-900 (CMP-Ts). The residues were washed with DI water to get the CMP-Ts for supercapacitor electrode.

Raman spectroscopy was used to characterize the structure of carbon materials (Fig. 2b). It can be seen from Raman spectrum that CMP-Ts has D (disordered) band near 1360 cm^{-1} and G (graphite) band near 1605 cm^{-1} . The D band corresponds to the A_{1g} vibration mode, which is due to structural defects, and the G band corresponds to the E_{2g} vibration mode, which is generated by the stretching of the C–C bond. The degree of disorder of CMP-Ts can be judged by the intensity ratio between D band and G band. The I_D/I_G values of CMP-700, CMP-800 and CMP-900 were 1.27, 1.20 and 0.99, respectively. This indicates that porous carbon material has a certain degree of graphitization [33, 34].

The porosities of CMP-Ts were characterized by N_2 adsorption/desorption isotherms at 77 K (Fig. 2c). It can be seen that the shape of the N_2 adsorption isotherm of CMP-Ts shows characteristic of a type-I isotherm [35]. At relatively low pressure, the adsorption capacity increases sharply, and

quickly reaches saturation, which confirms the existence of a large number of micropores in CMP-Ts. Combined with the pore size distribution, it revealed that CMP-Ts is a micropore and mesopore material [36] (Fig. 2d). The specific BET surface areas and the pore structure parameters were summarized in Table S1. The BET surface area of CMP was only $13.53 \text{ m}^2 \text{ g}^{-1}$, but it was drastically enlarged after activation, especially for CMP-800 ($2229.85 \text{ m}^2 \text{ g}^{-1}$). The ratio of micropore to total pore volume was also greatly increased after activation. The CMP-800 possess a higher ratio of micropore than those of CMP-700 and CMP-900.

The crystal structure of CMP-Ts was characterized by X-ray diffraction (XRD), as shown in Fig. 2e. Wide diffraction bands appear at about 23° and weak diffraction bands at about 43° , corresponding to the (002) and (100) crystal surfaces of graphite, respectively. At the same time, the significantly increased low angle scattering confirmed that the porous structure of the material was preserved after heat treatment, indicating that the porous carbon material has a certain degree of graphitization [37].

The XPS survey spectra (Fig. 2f) of the samples present two clear peaks at 285.0 and 532.0 eV, which corresponding to C 1s and O 1s, respectively. And the S 2p signal at 168.0 eV represents the C-S bond [38]. XPS peak spectrogram of CMP and CMP-800 were shown in Fig. S4, it can be clearly seen that CMP-800 maintains high O (6.57%) and S (2.96%) atomic contents, which proves that C, O and S elements are contained in the carbon material. The XPS spectra also indicate that the O and S atoms maintain their

chemical structures in the porous carbons successfully. And their atomic contents are shown in Fig. S5 and Table S2. The fitting peak of C 1s peak is located at 286.4 eV (C–O) and 284.6 eV (C–C). S 2p spectrum contains four peaks, representing three types of sulfur, S $2p_{3/2}$ (163.7 eV), S $2p_{1/2}$ (164.8 eV), and oxidized sulfur ($-\text{SO}_x$) (168.3 eV and 169.3 eV). For O 1s spectrum, the peak at 532.4 eV can be attributed to the C–O bond, and the peak at 533.7 eV corresponds to the binding energy of the oxygen-containing C–O–C functional group. These results indicate that oxygen-containing functional groups increase the wettability of the electrode surface, thus facilitating the entry and infiltration of electrolyte into the micropores [34]. At the same time, sulfur atoms successfully integrate into the carbon network and play an important role in improving the electrochemical performance of CMP-800.

The morphologies of CMP and CMP-Ts were studied by scanning electron microscopy (SEM). As shown in Fig. 3a, CMP is composed of many small and layered holes with uneven morphology (Fig. 3a), which indicates that layered CMP has been successfully synthesized. However, compared with the pore structure of carbonized CMP-700 (Fig. 3b), CMP-800 (Fig. 3c) and CMP-900 (Fig. 3d), these holes are more abundant and more obvious, which is caused by the activation of KOH in the process of high temperature carbonization. It is worth noting that the rich fold and porous structure of this series of carbon materials possess increased specific surface area and pore volume, providing more active sites for the charge accumulation and ion transport of ions.

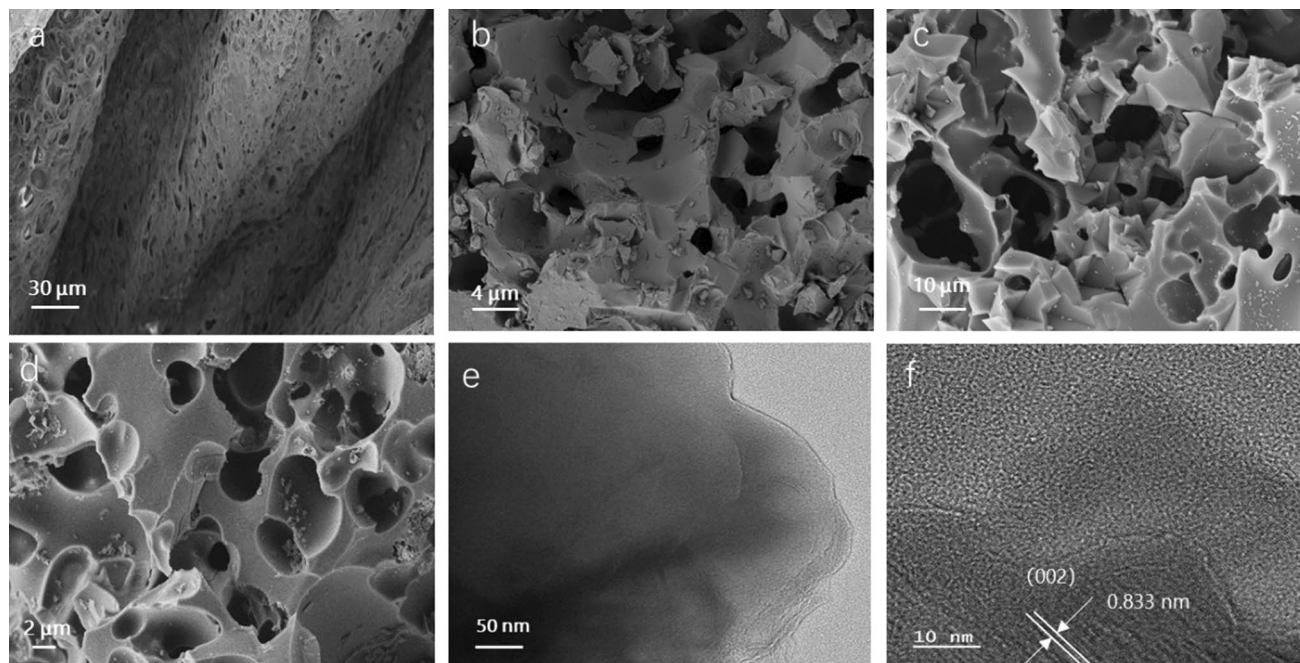


Fig. 3 SEM images of **a** CMP, **b** CMP-700, **c** CMP-800, **d** CMP-900; TEM image of **e** CMP-800, and HRTEM image of **f** CMP-800

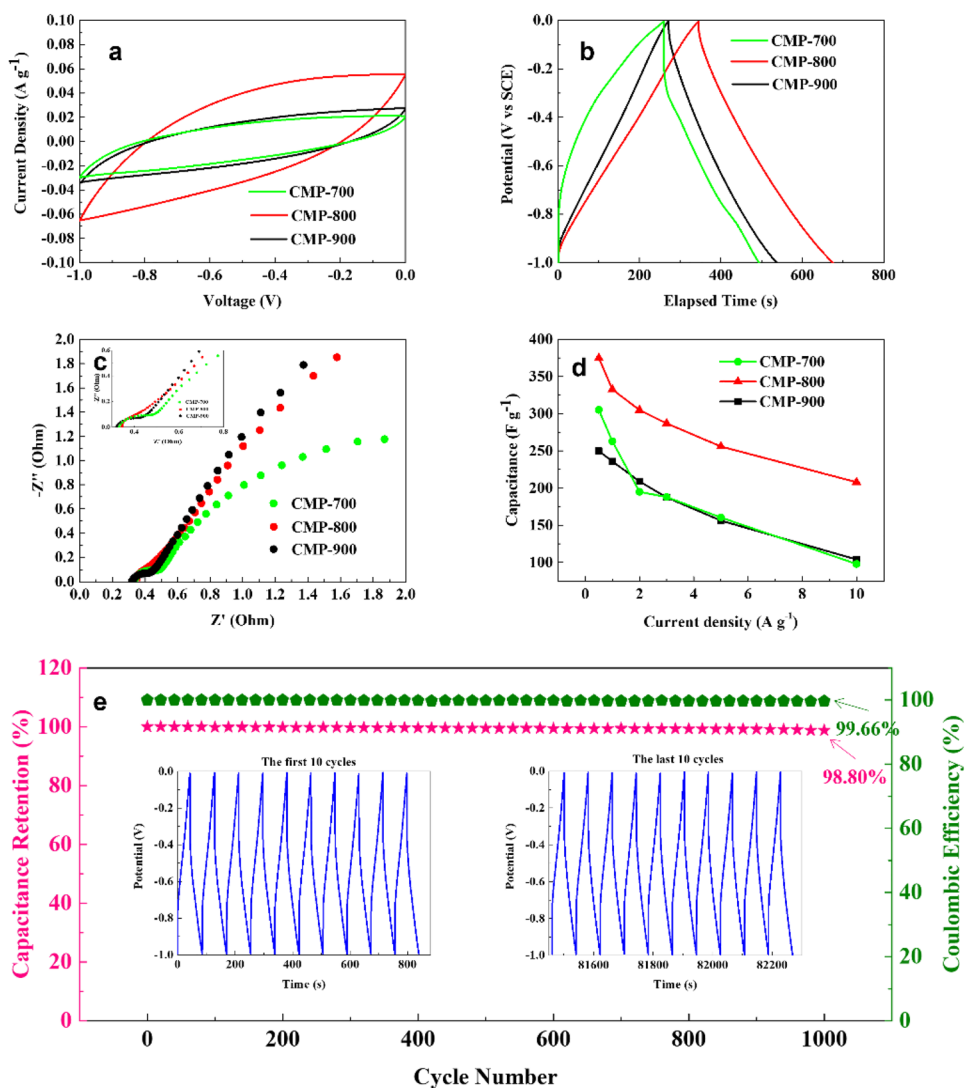
This is also in consistent with the excellent electrochemical performance of the prepared carbon materials. In addition, the CMP-800 were characterized by TEM in Fig. 3e. The observed particle size is in consistent with diameter value determined from XRD and surface area measurements. The high resolution transmission electron microscopy (HRTEM) in Fig. 3f confirms the CMP-800 with good crystallinity and thus corresponds well with the XRD results.

3.3 Electrochemical performance

The electrochemical performance of CMP-Ts in 6 M KOH aqueous solution was studied. The cell voltage window was $-1.0 \sim 0$ V. The cyclic voltammetry curves of CMP-700, CMP-800 and CMP-900 at 50 mV s^{-1} scan rate show a similar rectangular shape without any redox peaks (Fig. 4a), which is typical CV shape of electrochemical double-layer capacitors (EDLC) [30]. The slight bumps in these CV curves indicate that doped heteroatoms

participate in the redox reaction and generate partial pseudo-capacitance, further enhancing the capacitive performance and confirming the effective role of doped heteroatoms [38]. Among them, the contribution of pseudo-capacitance to the overall capacity was investigated in Figure S6-S8 [39]. With the increasing of scan rate, the pseudo-capacitance ratio also increased from 0.8% to 9.8% in the range of 0 to 100 mV/s . In addition, the CMP-800 has a large integral area, indicating that it has the highest specific capacitance. The excellent electrochemical performance is due to its unique porous structure, which enables rapid ion transport and diffusion. The micropore is the active site of ion adsorption, and the mesopore provides a channel for rapid ion transport. CV curves of CMP-700 and CMP-900 at different scanning rates of $5\text{--}100 \text{ mV s}^{-1}$ are shown in Fig. S9, S10. Even at very high scan rates, the CV shapes of CMP-Ts barely change, indicating that CMP-Ts has the ability of rapid

Fig. 4 **a** CV curves of CMP-Ts at a potential scan rate of 50 mV s^{-1} , **b** GCD curves of CMP-Ts at a current density of 1 A g^{-1} . **c** Nyquist plots (Inset: magnification of the high-frequency region), and **d** Magnification performance test diagram of CMP-Ts, **e** Cycling stability of CMP-800 at 5 A g^{-1} , (inset) GCD curves of the first and the last 10 cycles



ion diffusion and good charge stability as the electrode material for supercapacitors.

Figure 4b shows the constant current charge–discharge (GCD) of CMP-700, CMP-800, and CMP-900 samples respectively at the current density of 1 A g^{-1} . It can be seen from the figure that the charge-discharge curves of the three samples are in an isosceles triangle structure with good symmetry. The calculated specific capacitance is 236 F g^{-1} , 332.6 F g^{-1} and 305.2 F g^{-1} , respectively. The specific capacitance of CMP-800 is the highest, which is also in consistent with the results of cyclic voltammetry test. Figs. S11 and S12 show the GCD curves of CMP-700 and CMP-900 under different current densities respectively. The current densities used in the test are as follows: 0.5 A g^{-1} to 10 A g^{-1} . For a current density of 0.5 A g^{-1} , the specific capacitance can reach up to 375 F g^{-1} . It can be clearly seen from the figure that the discharge time of sample CMP-800 is the longest, and the specific capacitance of CMP-800 is the highest among the samples at different current densities. The results are in consistent with the cyclic voltammetry, and the well-maintenance of the triangular GCD profiles indicate the ideal capacitive behavior of CMP-800 which used as a promising material for energy-storage devices.

To obtain the best electrochemical properties, we have optimized the carbonization procedures. Among the different carbonization temperature, CMP-800 exhibits the largest specific capacitance of 332.6 F g^{-1} at a current density of 1 A g^{-1} (Fig. 4d). When the current density increased to 10 A g^{-1} , the capacitance of CMP-800 can be still maintained at 208 F g^{-1} , demonstrating a good capacitance retention capability. The ratio of KOH and CMP for activation was also optimized in Fig. 5c. When the ratio of KOH: CMPs is 2:1, the obtained material exhibits the highest capacitance.

Figure 4c shows the AC impedance maps of samples CMP-700, CMP-800, and CMP-900. The Nyquist diagram mainly consists of two parts: the semi-arc part in the high frequency region and the linear part in the low frequency region. The half-arc part represents the charge transfer resistance R_{ct} , and the smaller the half-arc diameter is, the smaller the charge transfer resistance is [40]. The linear part is related to the diffusion of electrolyte ions in the electrode material. The higher the slope, the faster the diffusion, and the faster the formation rate of double electric layer [41, 42]. In addition, the intercept between the semicircle and the X-axis in the high-frequency region represents the solution resistance R_s , which including the resistance of the electrode material itself, the electrolyte resistance and the contact resistance between the electrode and the fluid collector, etc. [43]. It can be seen from the figure that the R_s of CMP-800 is slightly smaller than CMP-700 and CMP-900, indicating that carbonization to $800 \text{ }^\circ\text{C}$ can effectively reduce the solution resistance of the sample. Meanwhile, in the linear part of the low

frequency region, the slopes of CMP-800 and CMP-900 are similar and significantly higher than that of CMP-700, indicating that electrolyte ions are diffused faster in electrode materials at carbonization temperatures of $800 \text{ }^\circ\text{C}$ and $900 \text{ }^\circ\text{C}$. This result is in consistent with the test results of constant current charge–discharge.

The cyclic stability of electrode material has great influence on the performance of supercapacitor. At present, most electrode materials based on organic materials and inorganic metal oxides are slightly inadequate in terms of cycle stability [44]. As shown in Fig. 4e, the cyclic stability of CMP-800 was tested for 1000 times of continuous charging and discharging at 5 A g^{-1} of current density. The results show that the specific capacitance remains almost constant during the test. The constant current charge–discharge curves of the last 10 cycles still maintain a symmetrical triangle (Fig. 4e), showing good long-term and stable cyclic performance. After 1000 cycles, the sample capacity retention rate is 98.8%, and the coulomb efficiency is as high as 99.66%, which is due to the carbonized material has good stability, high conductivity, large specific surface area and high porosity. In addition, after 10,000 cycles at 10 A g^{-1} current density, the capacity retention rate and coulomb efficiency are 96.3% and 98.26%, respectively (Fig. 5e).

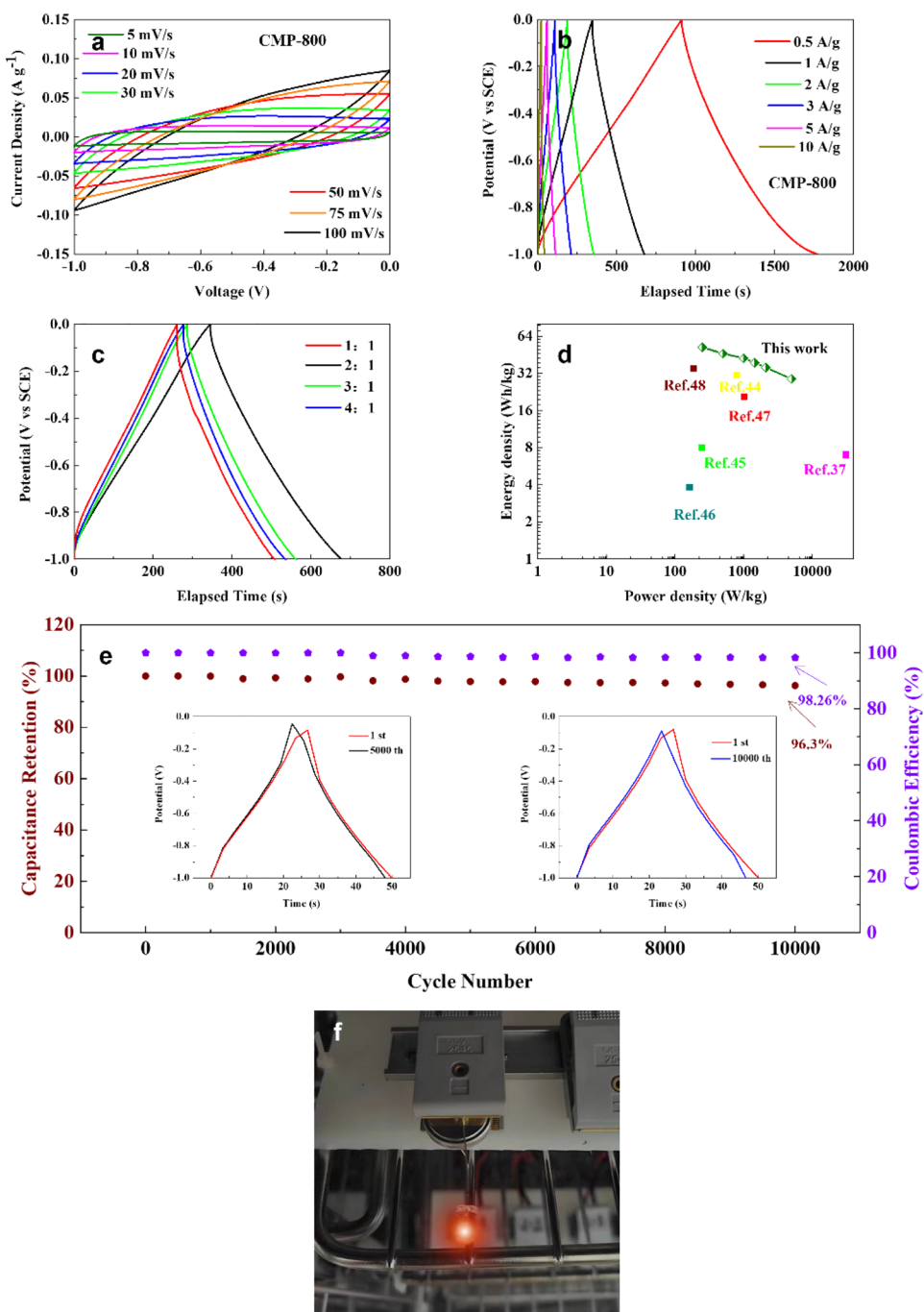
The power density and energy density of the supercapacitor (calculated by Eq. (3)) are measured and calculated in the dual-motor system, and the results are shown in the Ragone diagram (Fig. 5d) [35]. When the power density is 5000 W kg^{-1} , the energy density of CMP-800 reaches 28.8 Wh kg^{-1} , which is better than that of porous carbon materials previously reported [37, 44–48]. Meanwhile, two symmetrical snap supercapacitors in series can successfully light a small LED (2.0 V) bulb (Fig. 5f). In conclusion, CMP-800 has good electrochemical performance, and its specific surface area, porosity and heteroatom content achieve the best balance.

The constant-current charge–discharge curves (GCDs) of the electrode was tested in a three-electrode system, and the specific capacitance ($C, \text{ F}^{-1}$) was calculated by Eq. (1).

$$C = \frac{It}{mV} \quad (1)$$

where I is the discharge current, t is the discharge time, m is the mass of electrode active materials (working electrode), and V is the voltage window. In the two-electrode system, the mass specific capacity of the assembled supercapacitor ($C, \text{ F g}^{-1}$) was calculated from galvanostatic discharge curves based on Eq. (2), the energy density ($E, \text{ Wh kg}^{-1}$) and power capability ($P, \text{ W kg}^{-1}$) were obtained via Eqs. (3) and (4).

Fig. 5 **a** CV curves at different potential scan rates from 5 to 100 mV s⁻¹, **b** GCD curves at different current densities from 0.5 to 10 A g⁻¹, **c** GCD curves at different ratios of KOH and CMP-800 at 1.0 A g⁻¹, **d** Ragone plot (Energy density vs. Power density) and **e** Cycling stability at 10 A g⁻¹ of CMP-800, inset: the GCD curves of the 1st, 5000 th and 10,000 th cycles, **f** Image of a light-emitting LED powered by two buckle batteries



$$C = \frac{4It}{mV} \quad (2)$$

$$E = \frac{CV^2}{28.8} \quad (3)$$

$$P = \frac{3600E}{t} \quad (4)$$

where I is the discharge current, t is the discharge time, m is carbon material mass of electrode active materials, and V is the voltage window.

4 Conclusions

In summary, we have demonstrated a simple one-step coupling reaction method for the synthesis of CMPs as a precursor of heteroatomically doped porous carbon

(HPCs). The optimized CMP-800 electrode has a large specific surface area and high porosity, and a specific capacitance of 375 F g^{-1} when the current density is 0.5 A g^{-1} . When the power density is 5000 W kg^{-1} , the energy density is 28.8 Wh kg^{-1} . After 1000 cycles at 5 A g^{-1} current density, the capacity retention rate is maintained at 98.8% and the coulomb efficiency is maintained at 99.66%. These results open up a new way to synthesize HPCs and expand the application in high performance supercapacitors.

Supplementary Information The online version contains supplementary material available at <https://doi.org/10.1007/s42823-023-00553-9>.

Funding This study was financially supported by the Innovation Team Fund of University of Science and Technology Liaoning (2019TD01).

Data availability Additional data are made available in supplementary materials of this manuscript.

Declarations

Conflict of interest The authors declare that they have no known competing financial interests or personal relationships that could have appeared to influence the work reported in this paper.

References

- Koohi-Fayegh S, Rosen MA (2020) A review of energy storage types, applications and recent developments. *J Energy Storage* 27:101047–101069
- Halder A, Ghosh M, Khayum MA, Bera S, Addicoat M, Sasmal HS, Karak S, Kurungot S, Banerjee R (2018) Interlayer hydrogen-bonded covalent organic frameworks as high-performance supercapacitors. *J Am Chem Soc* 140:10941–10945
- Ciszewski M, Koszorek A, Radko T, Szatkowski P, Janas D (2018) Review of the selected carbon-based materials for symmetric supercapacitor application. *J Electron Mater* 48:717–744
- Wei J, Zhou D, Sun Z, Deng Y, Xia Y, Zhao D (2013) A controllable synthesis of rich nitrogen-doped ordered mesoporous carbon for CO_2 capture and supercapacitors. *Adv Funct Mater* 23:2322–2328
- Zhang Q, Han K, Li S, Ming L, Li J, Ke R (2018) Synthesis of garlic skin-derived 3D hierarchical porous carbon for high-performance supercapacitors. *Nanoscale* 10:2427–2437
- Béguin F, Presser V, Balducci A, Frackowiak E (2014) Supercapacitors: Carbons and electrolytes for advanced supercapacitors. *Adv Mater* 26:2219–2251
- Chen C, Wang H, Xiao Q, Zhao M, Li Y, Zhao G, Xie Y, Chen X, Zhu G (2019) Porous carbon hollow rod for supercapacitors with high energy density. *Ind Eng Chem Res* 58:22124–22132
- Díez N, Sevilla M, Fombona A, Pascual AB (2021) Monodisperse porous carbon nanospheres with ultra-high surface area for energy storage in electrochemical capacitors. *Batteries Supercaps* 5:1–11
- Liu C, Yu Z, Neff D, Zhamu A, Jang BZ (2010) Graphene-based supercapacitor with an ultrahigh energy density. *Nano Lett* 10:4863–4868
- Xu X, Gao J, Tian Q, Zhai X, Liu Y (2017) Walnut shell derived porous carbon for a symmetric all-solid-state supercapacitor. *Appl Surf Sci* 411:170–176
- Zhang X, Zheng W, Lu Y, Mai AYY, Liu JQ, Hua XL, Hao W (2018) Synthesis of core-shell covalent organic frameworks/multi-walled carbon nanotubes nanocomposite and application in lithium-sulfur batteries 17:31620–31628
- Zhou DD, Du YJ, Song YF, Wang YG, Wang CX, Xia YY (2013) Ordered hierarchical mesoporous/microporous carbon with optimized pore structure for supercapacitors. *J Mater Chem A* 1:1192–1200
- Yang LT, Zhu XZ, Li XH, Zhao XB, Pei K, You WB, Li X, Chen YJ, Lin CF, Che RC (2019) Conductive copper niobate: superior Li^+ -storage capability and novel Li^+ -transport mechanism. *Adv Energy Mater* 9:1902174–1902184
- Yang LT, Liang GS, Cao HJ, Ma SY, Liu XH, Li X, Chen GY, You WB, Lin CF, Che RC (2022) A new sodium calcium cyclotetranadate framework: “zero-strain” during large-capacity lithium intercalation. *Adv Funct Mater* 32:2105026–2105036
- Liang GS, Xiong XH, Yang LT, Liu XH, Che RC (2021) Zero-strain $\text{Ca}_{0.4}\text{Ce}_{0.6}\text{VO}_4$ anode material for high capacity and long-life Na-ion batteries. *J Mater Chem A* 9:25663–25671
- Liu CF, Liu YC, Yi TY, Hu CC (2018) Carbon materials for high-voltage supercapacitors. *Carbon* 145:529–548
- Yan D, Wu Y, Kitaura R, Awaga K (2019) Salt-assisted pyrolysis of covalent organic frameworks to porous heteroatom-doped carbons for supercapacitive energy storage. *J Mater Chem A* 7:26829–26837
- Kumar R, Sahoo S, Joanni E, Singh RK, Maegawa K, Tan WK, Kawamura G, Kar KK, Matsuda A (2020) Heteroatom doped graphene engineering for energy storage and conversion. *Mater Today* 39:47–65
- Liu Y, Liu Q, Wang L, Yang X, Yang W, Zheng J, Hou H (2020) Advanced supercapacitors based on porous hollow carbon nanofiber electrodes with high specific capacitance and large energy density. *ACS Appl Mater Interfaces* 12:4777–4786
- Rodrigues AC, Munhoz MGC, Pinheiro BS, Batista AF, Amaral-Labat GA, Cua A, Matsushima JT, Marcuzzo JS, Baldan MR (2020) N-activated carbon fiber produced by oxidation process design and its application as supercapacitor electrode. *J Porous Mater* 27:141–149
- Shin YS, Fryxell G, Um WY, Parker K, Mattigod SV, Skaggs R (2007) Sulfur-functionalized mesoporous carbon. *Adv Funct Mater* 17:2897–2901
- Yan XZ, Guan SY, Xiong YC, Wang Z, Chen H (2017) Boron and nitrogen co-doped porous carbon with a high concentration of boron and its superior capacitive behavior. *Carbon* 113:266–273
- Zhen Y, Miao Y, Huang JP, Xin XW, Yuan H, Sang H (2019) High-performance symmetric supercapacitor constructed using carbon cloth boosted by engineering oxygen-containing functional groups. *ACS Appl Mater Interfaces* 11:18044–18050
- Gopalakrishnan A, Badhulika S (2020) Effect of self-doped heteroatoms on the performance of biomass-derived carbon for supercapacitor applications. *J Power Sources* 480:228830–228846
- Liang Y, Lu Y, Xiao G, Zhang J, Chi H, Dong Y (2020) Hierarchical porous nitrogen-doped carbon microspheres after thermal rearrangement as high performance electrode materials for supercapacitors. *Appl Surf Sci* 529:147141–147151
- Demir M, Farghaly AA, Decuir MJ, Collinson MM, Gupta RB (2018) Supercapacitance and oxygen reduction characteristics of sulfur self-doped micro/mesoporous bio-carbon derived from lignin. *Mater Chem Phys* 216:508–516
- Liu S, Chen K, Wu Q, Gao Y, Xue C, Dong X (2022) Ulothrix-derived sulfur-doped porous carbon for high-performance symmetric supercapacitors. *ACS Omega* 7:10137–10143

28. Wang Y, Wang D, Li Z, Su Q, Wei S, Pang S, Zhao X, Liang L, Kang L, Cao S (2022) Preparation of boron/sulfur-codoped porous carbon derived from biological wastes and its application in a supercapacitor. *Nanomaterials* 12:1182–1196
29. Xu G, Yang G, Wang Y, Shao PL, Yau JNN, Liu B, Zhao Y, Sun Y, Xie X, Wang S, Zhang Y, Xia L, Zhao Y (2019) Stereoconvergent, redox-neutral access to tetrahydroquinoxalines through relay epoxide opening/amination of alcohols. *Angew Chem Int Ed Engl* 58:14082–14088
30. Zhao Y, Bu N, Shao H, Zhang Q, Feng B, Xu Y, Zheng G, Yuan Y, Yan Z, Xia L (2019) A carbonized porous aromatic framework to achieve customized nitrogen atoms for enhanced supercapacitor performance. *New J Chem* 43:18158–18164
31. Zhao Y, Yuan Y, Xu Y, Zheng G, Zhang Q, Jiang Y, Wang Z, Bu N, Xia L, Yan Z (2021) Fine-regulating ultramicropores in porous carbon via a self-sacrificial template route for high-performance supercapacitors. *Nanoscale* 13:1961–1969
32. Xie K, Qin X, Wang X, Wang Y, Tao H, Wu Q, Yang L, Hu Z (2012) Carbon nanocages as supercapacitor electrode materials. *Adv Mater* 24:347–352
33. Wen ZB, Qu QT, Gao Q, Zheng XW, Hu ZH, Wu YP, Liu YF, Wang XJ (2009) An activated carbon with high capacitance from carbonization of a resorcinol–formaldehyde resin. *Electrochem Commun* 11:715–718
34. Zhang W, Xu J, Hou D, Yin J, Liu D, He Y, Lin H (2018) Hierarchical porous carbon prepared from biomass through a facile method for supercapacitor applications. *J Colloid Interface Sci* 530:338–344
35. Liang J, Xiao Z, Gao Y, Xu X, Kong D, Wagner M, Zhi L (2019) Ionothermal strategy towards template-free hierarchical porous carbons for supercapacitive energy storage. *Carbon* 143:487–493
36. Li T, Yan X, Liu Y, Zhang W-D, Fu QT, Zhu H, Li Z, Gu ZG (2020) A 2D covalent organic framework involving strong intramolecular hydrogen bonds for advanced supercapacitors. *Polym Chem* 11:47–52
37. Jiang L, Sheng L, Long C, Wei T, Fan Z (2015) Functional pillared graphene frameworks for ultrahigh volumetric performance supercapacitors. *Adv Energy Mater* 5:1500771–1500779
38. Gogotsi Y, Penner RM (2018) Energy storage in nanomaterials—capacitive, pseudocapacitive, or battery-like? *ACS Nano* 12:2081–2083
39. Wang J, Polleux J, Lim J, Dunn B (2007) Pseudocapacitive contributions to electrochemical energy storage in TiO_2 (anatase) nanoparticles. *J Phys Chem C* 111:14925–14931
40. Yang L, Cheng S, Ding Y, Zhu XB, Wang ZL, Liu ML (2012) Hierarchical network architectures of carbon fiber paper supported cobalt oxide nanonet for high-capacity pseudocapacitors. *Nano Lett* 12:321–325
41. Wang H, Wang H, Ruan F, Feng Q, Wei Y, Fang J (2023) High-porosity carbon nanofibers prepared from polyacrylonitrile blended with amylose starch for application in supercapacitors. *Mater Chem Phys* 293:126896–126906
42. Hassan FM, Chabot V, Li J, Kim BK, Ricardez-Sandoval L, Yu A (2013) Pyrrolic-structure enriched nitrogen doped graphene for highly efficient next generation supercapacitors. *J Mater Chem A* 1:2904–2912
43. Ferrero GA, Fuertes AB, Sevilla M (2015) N-doped porous carbon capsules with tunable porosity for high-performance supercapacitors. *J Mater Chem A* 3:2914–2923
44. Chen N, Zhou J, Zhu G, Kang Q, Ji H, Zhang Y, Wang X, Peng L, Guo X, Lu C, Chen J, Feng X, Hou W (2018) A high-performance asymmetric supercapacitor based on vanadyl phosphate/carbon nanocomposites and polypyrrole-derived carbon nanowires. *Nanoscale* 10:3709–3719
45. Ni G, Qin F, Guo Z, Wang J, Shen W (2020) Nitrogen-doped asphaltene-based porous carbon fibers as supercapacitor electrode material with high specific capacitance. *Electrochim Acta* 330:135270–135283
46. Guo H, Gao Q (2009) Boron and nitrogen co-doped porous carbon and its enhanced properties as supercapacitor. *J Power Sources* 186:551–556
47. Cheng J, Lu Z, Zhao X, Chen X, Liu Y (2021) Green needle coke-derived porous carbon for high-performance symmetric supercapacitor. *J Power Sources* 494:229770–229779
48. Deng Y, Ji Y, Wu H, Chen F (2019) Enhanced electrochemical performance and high voltage window for supercapacitor based on multi-heteroatom modified porous carbon materials. *Chem Commun* 55:1486–1489

Publisher's Note Springer Nature remains neutral with regard to jurisdictional claims in published maps and institutional affiliations.

Springer Nature or its licensor (e.g. a society or other partner) holds exclusive rights to this article under a publishing agreement with the author(s) or other rightsholder(s); author self-archiving of the accepted manuscript version of this article is solely governed by the terms of such publishing agreement and applicable law.